A Simple Multi-Parametric Quantitative MRI Phantom

by

William T. Reichert

Thesis

submitted to the Faculty of the

Graduate School of Vanderbilt University

in partial fulfillment of the requirements

for the degree of

MASTER OF SCIENCE

in

Biomedical Engineering

June 30, 2021

Nashville, Tennessee

Approved:

Mark D. Does, Ph.D.

Adam W. Anderson, Ph.D.

Table of Contents

List of Figures

List of Tables

Chapter 1. INTRODUCTION

1.1 Background and Purpose

Quantitative magnetic resonance imaging (qMRI) researchers design and implement MRI encoding techniques to report on the structure, composition, and status of tissue on the microscopic scale. Such encoding techniques, known simply as qMRI methods, commonly target longitudinal (T_1) and transverse (T_2) relaxation, water diffusion, or magnetization transfer in tissue. The development and assessment of techniques to probe these features is aided by the use of phantoms—synthetic chemical systems which exhibit known, controlled MRI characteristics.

Several well-defined chemical phantoms exist for reproducible, tunable, and tissue-relevant T_1 and T_2 [1–3], diffusion [4, 5], and magnetization transfer behavior [6], but options for more complex systems are limited. Dairy cream [7] and aqueous urea [8] have been used bi-exponential T_2 phantoms. Urea and water solutions have been used to mimic two-site exchange [9] and subsequently used for bi-exponential T_2 with exchange [8], but none of these systems incorporate options for diffusion or magnetization transfer. Recently, the Standards for Quantitative Magnetic Resonance committee has posited that a system phantom capable of simultaneously replicating several if not all of these qMRI parameters is necessary to ensure that qMRI measurements are comparable between scans, sites, and vendors over time [10]. The currently available NIST/ISMRM system phantom (caliberMRI, Boulder CO) has become the standard for clinical MRI systems, allowing researchers to assess T_1, T_2, and proton density in addition to image uniformity and geometric distortions [11, 12]. A separate NIST phantom developed in collaboration with the National Cancer Institute (NCI) and the Radiological Society of North America (RSNA) has likewise become the standard for diffusion qMRI [13].

While the NIST system phantom is well-characterized and has been widely adopted for research on clinical MRI systems, its size is incompatible with most animal systems and it lacks a tissue-relevant magnetization transfer effect. As such, the need remains for a system phantom which can be

inexpensively produced at any research institution and customized to fit smaller bore systems. Furthermore, a single phantom system which also incorporates a tissue-relevant magnetization transfer effect and restricted diffusion of water would be more than a convenience. A sequence designed to measure one parameter (e.g., T_1) may be sensitive to variations in another tissue characteristic (e.g., magnetization transfer). Likewise, model based qMRI methods, such as MR Fingerprinting, rely on having an accurate signal model. Calibrating and standardizing such a method on a model that does not reflect the signal characteristics of tissue may lead to a biased method and/or false confidence in its accuracy or precision.

The objective of this work is to introduce and characterize a family of qMRI phantoms that can be tuned to exhibit mono- and multi-exponential longitudinal and transverse relaxation, water diffusion within the range of many tissues, and magnetization transfer between water and macromolecular protons. The constituent chemicals and preparation scheme are introduced below.

1.2 Polyvinylpyrrolidone and Bovine Serum Albumin

Polyvinylpyrrolidone (PVP) is a linear water-soluble polymer commonly used in pharmaceutical products, adhesives, and cosmetics. It has been labeled a non-hazardous substance by the Occupational Safety and Health Administration (OSHA) and is relatively inexpensive as an MRI phantom material. In the context of qMRI, aqueous PVP solutions are well-established as phantoms for restricted diffusion studies [14]. At standard bore temperature, phantoms consisting of 40 to 45 % PVP by mass are capable of mimicking the restricted diffusion of water found in patients suffering from ischemic stroke.

Bovine serum albumin (BSA) is a protein used in drug delivery and cell culture applications due to its low cost and non-hazardous nature. Aqueous solutions of BSA have been used as qMRI phantoms for studies involving chemical exchange saturation transfer (CEST) and magnetization transfer (MT) sequences [6]. Cross-linked BSA, in particular, is a widely used chemical phantom for quantitative magnetization transfer (qMT) studies.

1.3 Phantom Preparation Scheme

Figure 1.1 illustrates the phantom preparation process. Briefly, PVP powder and BSA powder are mixed with deionized water, and then the BSA is cross-linked via microwave irradiation or other means. The PVP and BSA weight fractions may vary 5 to 20% and 10 to 20%, respectively. The PVP reduces water diffusion and introduces a second signal component with relatively short T_2 (similar to the myelin water signal seen in nerve and white matter). The cross-linked BSA provides a macromolecular proton pool that exchanges magnetization with water protons in a manner similar to that in tissue. In the case that no BSA is included in the phantom, reduction of the long-T_2 signal component into the desired range can be achieved through the addition of $MnCl_2$. This scheme allows any phantom within the ranges specified to be developed in under 24 hours and with lab equipment readily available in most research institutions.

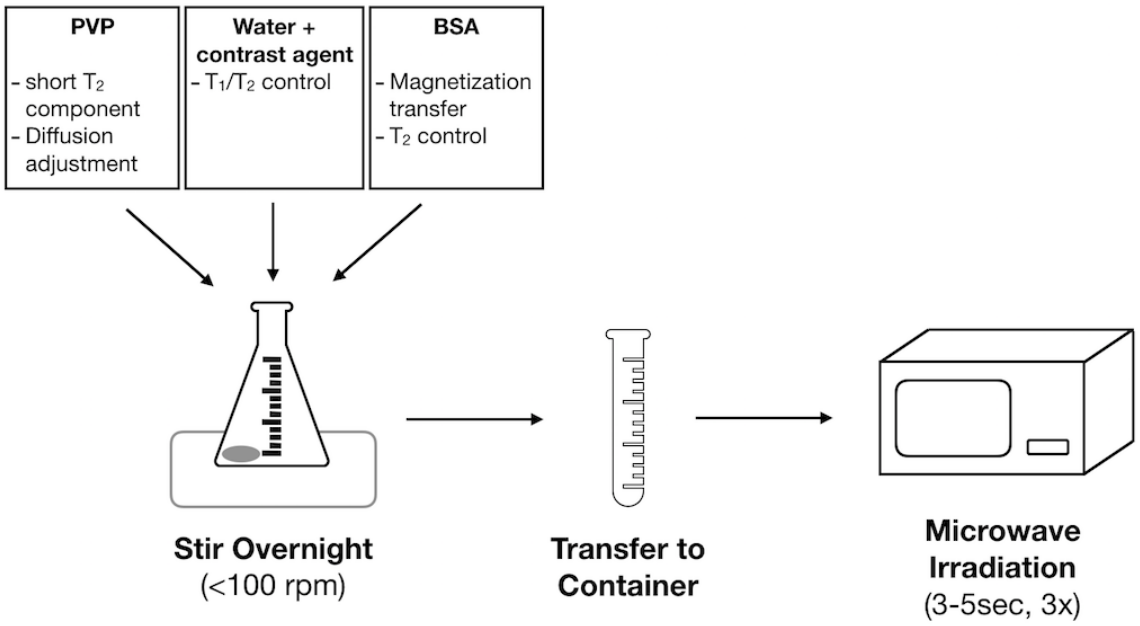

Figure 1.1: General schematic of the PVP:BSA phantom preparation process. PVP and BSA powder are gently stirred in water overnight, transferred into a suitable imaging container, and subjected to microwave irradiation at 700 W to cross-link.

1.4 Quantitative MRI Methods and Pulse Sequences

As mentioned previously, some of the most common parameters targeted in qMRI studies are T_1 and T_2 relaxation times, apparent diffusion of water, and the quantity of macromolecular protons which exchange magnetization with water. This section will briefly introduce these parameters and some of the qMRI methods used to measure them, with emphasis paid to the pulse sequences used in this work.

1.4.1 Relaxometry

Relaxometry is the name given to the study of proton relaxation under MR. In a static magnetic field (B_0), the net magnetization of protons aligns with the field, in what is termed the longitudinal (z) direction. After a radiofrequency (RF) pulse excites, inverts, or otherwise disturbs this magnetization, the system's spins exchange energy with their environment and the net magnetization vector returns to its equilibrium alignment along B_0. The longitudinal (T_1) relaxation time constant is associated with the rate at which magnetization is restored along the longitudinal direction, while the transverse (T_2) relaxation time constant is associated with the rate at which magnetization in the transverse plane decays. T_2 relaxation may be accelerated by local field disturbances, chemical exchange, or dipolar interactions which disturb phase coherence, resulting in a loss of net transverse relaxation. As such, T_2 relaxation is always faster than or at least equivalent to T_1 relaxation. In more complex physical systems, protons in different chemical environments relax at different rates, resulting in a distribution of T_1 and T_2 relaxation times. One example observable in tissue is signal from water trapped between layers of the myelin sheath observed in the central nervous system, dubbed "myelin water." These water molecules interact much more closely with myelin macromolecules, and have a characteristically short T_2 (15 to 30 ms).

Quantitative MRI methods characterize systems with multiple T_2 components by acquiring signal at several time points after excitation and fitting the data to a sum of exponential decay functions. The gold standard for multi-exponential T_2 characterization in imaging systems is the multiple spin echo (MSE) pulse sequence, an imaging adaptation of the Carr-Purcell-Meiboom-Gill (CPMG) NMR

sequence. Both sequences share the following protocol. First, a 90° excitation pulse tips all magnetization into the transverse plane, and magnetization begins dephasing. After a time ΔTE/2, a 180° (refocusing) pulse inverts the phase of all transverse magnetization; after another ΔTE/2 delay, the magnetization has been rephased, producing an echo. At this time, signal is acquired, the magnetization continues dephasing, and after another ΔTE/2 delay a second refocusing pulse plays out. This sequence—refocusing pulse, delay, echo, delay, refocusing pulse—is repeated to acquire data at multiple echo times after excitation. Provided that enough time passes between each sequence repeat for magnetization to reach thermal equilibrium (i.e. the repetition time T_R is long enough), the acquired data may then be fitted to a multi-exponential equation like Eq. 1.1 below. Here, the signal measured at time TE is represented as the sum of M components, each with its own signal amplitude S_0 and T_2 relaxation time. The list of fitted signal components and associated T_2 relaxation times may be plotted against one another to generate a spectrum of the system's T_2 distribution.

$$S(TE_i) = \sum_{j=1}^{M} S_{0,j} e^{-TE_i/T_{2,j}} \tag{1.1}$$

T_1 can be measured with an inversion recovery sequence. In such a sequence, magnetization is inverted with an RF pulse and allowed to recover for a set period, known as the inversion time. Subsequently, the signal is excited and recorded, and the process is repeated for several inversion times. If $T_R >> T_1$, the acquired data may then be fitted to a T_1 signal recovery model, as described below.

$$S(T_\mathrm{I}) = S_0[1 - (1 - \cos(\alpha))e^{-T_\mathrm{I}/T_1}] \tag{1.2}$$

Here, $S(T_\mathrm{I})$ is the signal measured at inversion time T_I, S_0 is the equilibrium magnetization, and α is the flip angle of the inversion pulse. T_1 and multi-exponential T_2 may be characterized simultaneously by combining the methods described above; by placing an inversion pulse and variable inversion time before the CPMG's excitation pulse, one sequence may be used to measure both T_1 and T_2.

1.4.2 Diffusometry

The apparent diffusion of water molecules is commonly measured using a pulsed gradient spin echo (PGSE) sequence. A typical DWI pulse sequence applies two equivalent gradients after excitation, separated from one another by the diffusion time Δ and a 180° refocusing pulse. In the absence of diffusion, the refocusing pulse (or reversed polarity of the second gradient) causes the gradient effects to cancel out, leaving no effect on the signal. If protons diffuse from one location to another before the second gradient plays out, however, the two gradients' effects will not fully cancel, dephasing the protons and reducing signal. The gradients are altered after an image is acquired, changing the effect of location-dependent signal attenuation. Typically, one image is acquired without any diffusion gradients, while all others are acquired at varying gradient strengths. The data is then fit to a signal decay function, the most simple of which is described below:

$$S(b) = S_0 e^{-bD} \tag{1.3}$$

Here, S_0 is the signal acquired with no diffusion gradients, D is the apparent diffusion coefficient of water, and b is the b-value, an independent variable dependent on the gradient strength (G), duration (δ), and the spacing between diffusion gradients (Δ). In a PGSE sequence, the b-value is defined as

$$b = (\gamma G \delta)^2 (\Delta - \delta/3). \tag{1.4}$$

1.4.3 Magnetization Transfer

Magnetization transfer refers to the process by which energy obtained from an RF pulse is exchanged between macromolecular protons (the "bound pool") and neighboring water signal (the "free pool"). This exchange can occur via dipole-dipole interactions and chemical exchange between the two pools. Quantitative magnetization transfer (qMT) methods attempt to model this exchange process, including the size of the macromolecular pool and rate of exchange. Two of the most well-known qMRI methods used in developing exchange models are offset qMT and selective inversion recovery.

Offset qMT is the most widely adopted method; several modifications and specialized sequences exist for specific tissue types, but the general methodology is to apply a pulse or series of pulses off resonance from water. This pulse saturates the bound pool magnetization with minimal effect on water magnetization. Following this, an excitation-acquisition sequence is played. Magnetization transfer may be inferred from the decrease in water magnetization observed using this sequence compared to that observed in the absence of any off-resonance saturation. A typical qMT study will include repeated acquisition with multiple MT pulses at varying powers and offset frequencies. The model will vary depending on the specific sequence used.

Selective inversion recovery (SIR) is another qMT method which probes the system by primarily disturbing the free water magnetization. A low-power inversion pulse is played to invert water protons with minimal effect on the macromolecular protons. During recovery, water protons will exchange longitudinal magnetization with the lower energy state macromolecular protons, resulting in a bi-exponential signal recovery curve. As with offset qMT modeling, fitting data to the signal recovery curve yields measures of the bound pool's size and the exchange rate between pools.

Chapter 2. MATERIALS AND METHODS

Two sets of phantoms were developed and characterized: 1) a set of aqueous PVP phantoms ranging from 10 to 40 wt% PVP and 0 to 80 µM $MnCl_2$, and 2) a set of 5 to 20 wt% PVP with 10 to 20 wt% BSA phantoms, cross-linked via microwave irradiation. Both phantom sets were studied with non-localized relaxation and magnetization transfer measurements at 400 MHz. Additionally, all phantoms were scanned on a 7 T imaging system at 23 °C to characterize water diffusion. The following sections provide further detail on phantom preparation, imaging, and data analysis.

2.1 Phantom Preparation

For the PVP phantoms, glass beakers were filled with PVP powder (PVP, avg. molecular weight 40,000; Sigma-Aldrich Corp) and de-ionized water and then sealed with aluminum foil. Mixtures were lightly stirred (≤ 100 rpm) on a magnetic stir plate overnight, and then transferred to 50 mL Falcon tubes and sealed for storage. Three such 40% stocks were made independently. Each stock was then separated into 15 mL Falcon tubes and diluted with de-ionized water to obtain solutions spanning 10 to 40% PVP by mass. An additional series of phantoms were prepared by mixing solutions of 10% PVP with manganese (II) chloride tetra-hydrate ($MnCl_2 \cdot 4H_2O$, Sigma-Aldrich), with Mn concentrations varying 0 to 80 µmol/L.

For the PVP and BSA phantoms, various amounts of PVP and BSA powders were combined in glass beakers and mixed before the addition of de-ionized water. The beakers were sealed with foil and gently rocked for 15 minutes to mitigate BSA aggregation and foaming, and then left on a magnetic stir plate overnight (≤ 100 rpm). Solutions were cross-linked via three doses of microwave irradiation at 700 W for 3 to 5 s each. Irradiation treatments were spaced one minute apart to prevent excessive heating and mitigate the formation of trapped air bubbles. The PVP:BSA phantom compositions ranged 0 to 20% PVP and 5 to 20% BSA, limited on one end by the BSA concentration needed to successfully cross-link the phantom and on the other by the chemicals' solubility in water.

2.2 ^{1}H NMR

Non-localized ^{1}H NMR measurements were used for chemical shift, relaxometry, and magnetization transfer measurements at 9.4 T. All ^{1}H NMR studies were conducted at approximately 23 °C on a 400 MHz Bruker Avance III spectrometer equipped with TopSpin 3.0 software. Chemical shift spectra were obtained with a spin-echo-prepared–FID sequence, run with ~ 8.5 µs and ~ 17 µs duration excitation and refocusing pulses, respectively, 8192 samples acquired at 4 kHz (10 ppm) bandwidth, 6 averaged excitations (N_{ex}), a 10 s pre-delay time (T_d), and a repeated with the following echo times (T_E) = 2, 10, 20, 50, 100 and 200 ms. Bulk T_1- and T_2-relaxation studies were conducted using an inversion recovery (IR) prepared Carr-Purcell-Meiboom-Gill (CPMG) sequence with the following parameters: 1000 echoes (N_E), uniform echo spacing (τ_e) = 4 ms, 15 inversion delays (T_I) log-spaced from 5 ms to 10 s, N_{ex} = 4, T_d = 10 s, and a four-step phase cycling scheme ($90_{x,-x,x,-x}$, $180_{y,y,-y,-y}$). To investigate magnetization transfer, the IR-CPMG measurements were repeated using low-bandwidth inversion pulses, 1.5 ms duration. (This method is referred to as selective inversion recovery, SIR). A subset of phantoms—15 wt% PVP, 15 wt% BSA—was also scanned using an off-resonance qMT sequence similar to the one described by Henkelman et al [15]. A 5 s saturation pulse with amplitude 0.67 kHz was applied at 25 frequencies, log-spaced from 50 Hz to 200 kHz off-resonance from the water signal peak in either direction. Finally, further characterization of transverse relaxation in 40 wt% PVP was carried out with CPMG acquisitions using N_E = 10 000, τ_e = 50 µs, 100 µs, or 1 ms, and N_{ex} = 16.

2.3 MRI

All diffusion studies were performed on a 7 T-16 cm horizontal-bore magnet equipped with a Bruker Biospec console (Rheinstetten, Germany), operated with ParaVision 6.0.1 software. Diffusion-weighted MRI with varied T_2-weighting were acquired at using pulsed gradients (Δ = 8 ms, δ = 5 ms) followed by a multiple spin echo (MSE) readout, N_E = 10, τ_e = 10 ms, T_E = 20 to 110 ms. Images were encoded with a 64 × 64 matrix over a 30 mm × 30 mm FOV, with a 2 mm slice thickness, T_R = 3 s, and N_{ex} = 2. For PVP samples, which included diffusion coefficients as low as ≈ 0.6 µm^2/ms, acquisi-

tions were repeated with 7 b-values, $b = 0$, 0.5, 1, 2, 3, 4 and 6 ms/μm^2. For the PVP+BSA samples, diffusion was greater and so only b-values up to 3 ms/μm^2 were used ($b = 0$, 0.5, 1, 2 and 3 ms/μm^2).

2.4 Data Analysis

Chemical shift spectra were generated by taking the Fourier transform of the acquired FID signals and applying first-order phase correction. Shift corrections were applied to set the chemical shift of the majority signal peak attributable to water signal at 4.8 ppm. The signal amplitudes of bulk water and all chemically shifted signal across all measured echo times were fitted to a mono-exponential decay to approximate T_2 in the two components.

All non-localized multi-exponential T_2 relaxometry characterization was performed on the equilibrium signal magnitudes of 2D IR-CPMG measurements, approximated as the signal acquired at the longest inversion time. The equilibrium signal was fitted in a nonnegative least-squares sense to the sum of 200 exponential functions with logarithmically-spaced time constants spanning each study's first to final echo times, and subject to minimum curvature regularization [16]. Following this, signal was split into two components by a T_2 cutoff of 30 ms; all signal with T_2 shorter than the cutoff was identified as pool B, while all signal with a longer T_2 was labeled pool A. T_{2a} and T_{2b} were calculated as the geometric mean T_2 from all signal within each assigned pool. Signal fractions f_a and f_b were calculated as the sum of all fitted signal amplitudes within each pool divided by the total signal in both pools.

T_{1a} and T_{1b} were then calculated via mono-exponential analysis of each signal component (as previously defined by T_2). First, all complex signals were subtracted from equilibrium signal to remove unwanted phase and B_1 effects, resulting in decaying signal arrays. For each T_I, the subtracted signal magnitudes were first fitted to T_2 spectra using the same nonnegative least-squares analysis described for T_2 fitting. T_{1a} and T_{1b} were calculated by fitting the total signal in each pool—defined by the T_2 cutoff established prior—across all T_I to a mono-exponential T_1 decay.

Diffusion-weighted image magnitudes, S, at each echo time, t, and diffusion-weighting b-value

were fitted to a bi-exponential signal model,

$$S(b,t) = S_0 \left[f_\mathrm{a} e^{-tR_{2,\mathrm{a}}} e^{-bD_\mathrm{a}} + (1-f_\mathrm{a}) e^{-tR_{2,\mathrm{b}}} e^{-bD_\mathrm{b}} \right] \tag{2.1}$$

with two signal components labeled as 'a' and 'b', with signal fractions f_a and $1-f_\mathrm{a}$, and each with a unique transverse relaxation rate, $R_{2,\mathrm{a/b}}$, and apparent diffusion coefficient, $D_\mathrm{a/b}$. Parameter f_a was set for each concentration as the signal fraction obtained from T_2 data analysis at 400 MHz, while $R_{2\mathrm{a}}$ and $\mathrm{R}_{2\mathrm{b}}$ were fitted as free parameters since their values on the 7 T system may differ from those observed at 400 MHz. R_2 fitting was subject to the restriction that $R_{2,\mathrm{b}} > R_{2,\mathrm{a}}$. Mono-exponential analysis was also performed by constraining $f_\mathrm{a} = 1$, and then an F-test was used to determine which signal model best described the data. The apparent diffusion coefficient of water D_a as fitted using Eq 2.1 was used in all subsequent data analysis to develop the phenomenological model for diffusion, detailed later.

Selective inversion recovery data were fitted to a two-pool model (water and macromolecular protons) described by coupled Bloch equations [17, 18]. The fraction of macromolecular proton magnetization, referred to here as the bound pool fraction (BPF, f_m), was fitted at the first echo time, T_E = 4 ms. Off-resonance qMT signal was divided by the equilibrium magnetization—approximated as the signal at the greatest offset frequency—and plotted against frequency offset in either direction.

Finally, phenomenological models relating relaxation rates, signal fraction in pool b, bound pool fraction, and apparent diffusion coefficient to phantom composition were generated via multiple linear regression analysis using MATLAB's stepwiselm function. Equation 2.2 below illustrates the model equation template:

$$Y = C_0 + C_\mathrm{P} X_\mathrm{PVP} + C_\mathrm{B} X_\mathrm{BSA} \tag{2.2}$$

Each qMRI parameter Y is described as a function of the weight fractions of PVP (X_PVP) and BSA (X_BSA). The SSE criterion was used in all cases under default settings ($p < 0.05$ significance required to add a term), and interaction terms were allowed.

Chapter 3. RESULTS

3.1 PVP

Before presenting the comprehensive phantom model, it is helpful to understand the role of PVP in solution. Representative ^{1}H NMR spectra for aqueous PVP are displayed in Figure 3.1. Several chemically shifted signal peaks can be observed; these signals are attributable to protons on the PVP polymer chain. The bulk water signal (4.8 ppm) decays over time with T_2 approximately 370 ms, while the shifted signal decays much more quickly ($T_2 \approx 8.5$ ms). Example T_2 spectra from solutions with various PVP concentrations are displayed in Fig 3.2; each spectrum can be split into a majority component with $T_2 > 100$ ms (pool A) and a range of peaks with T_2 ranging from 1 to 40 ms (pool B). Thus, the role of PVP in the phantom presented in the next section is to create a short-lived T_2 component, similar to the myelin water signal seen in neuronal tissue, in addition to reducing water diffusion to tissue-relevant levels, as previously demonstrated.

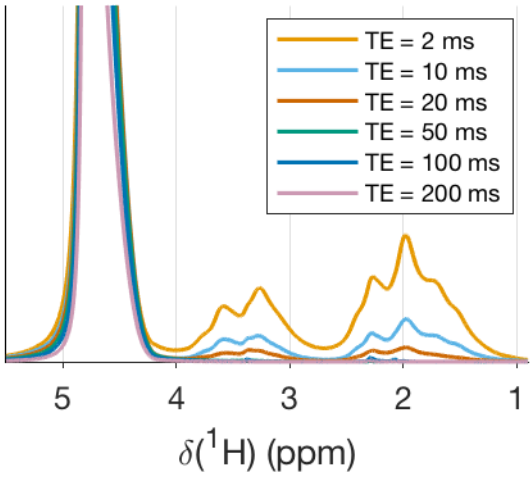

Figure 3.1: ^{1}H NMR spectra of 20 wt% PVP in water from FIDs acquired at TE ranging from 2 to 200 ms after excitation.

To this model, $MnCl_2$ can be added to reduce the long-lived T_2 component to tissue-relevant values. These results and a complete 2-compartment model of relaxation and diffusion in this phantom are presented in Appendix A, while tables containing all recorded qMRI parameters for aqueous PVP

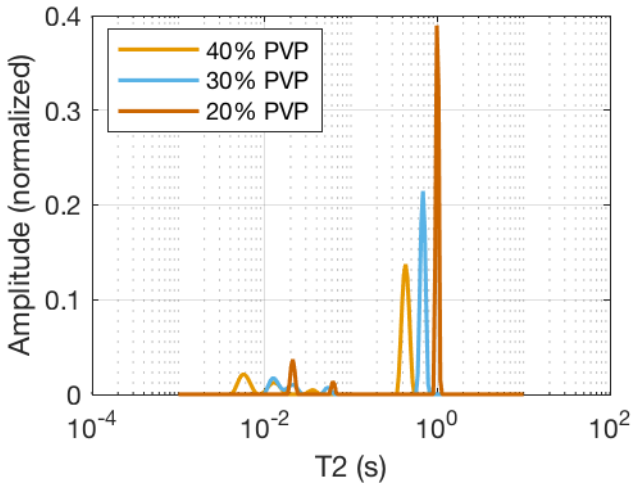

Figure 3.2: Representative normalized T_2 spectra of 40, 30, and 20 wt% aqueous PVP. Short-lived PVP proton signal accounts for 29.4%, 21.6%, and 14.1% of the total signal in each phantom, respectively.

can be found in Appendix B. For a more complete phantom that includes a magnetization transfer effect, the addition and cross-linking of BSA is necessary.

3.2 PVP:BSA

The addition of BSA and subsequent thermal cross-linking has multiple effects on the MR characteristics of the phantom. This section will address each qMRI parameter individually before presenting an overall system model, including equations relating each model parameter to PVP and BSA concentrations.

3.2.1 Individual qMRI Parameters

As seen in Fig 3.3, the relaxation characteristics of the PVP:BSA phantom are also well described by a two-compartment model, but now the long-lived signal component is within the tissue relevant range (without the need for a paramagnetic contrast agent). PVP and BSA play distinct roles with respect to the phantoms' multi-exponential T_2 behavior. Figure 3.4 illustrates the effect of changing PVP or BSA composition individually on the phantoms' T_2 spectra. The T_{2a} relaxation time depends primarily on BSA concentration, while the proportion of signal belonging to the short-lived pool f_b

depends primarily on PVP composition. In contrast, PVP and BSA both significantly contribute to the bulk water T_1. Figure 3.5 displays the trend between phantom composition and R_1 (= $1/T_1$) relaxation rate at 9.4 T. Here, PVP and BSA concentration are both linearly correlated to R_{1a} (R^2 = 0.84). Mono-exponential T_{1a} fits show good agreement with the data (Fig 3.6). The sum of squared residuals of each T_1 fit across concentrations averages under 0.003 (normalized units).

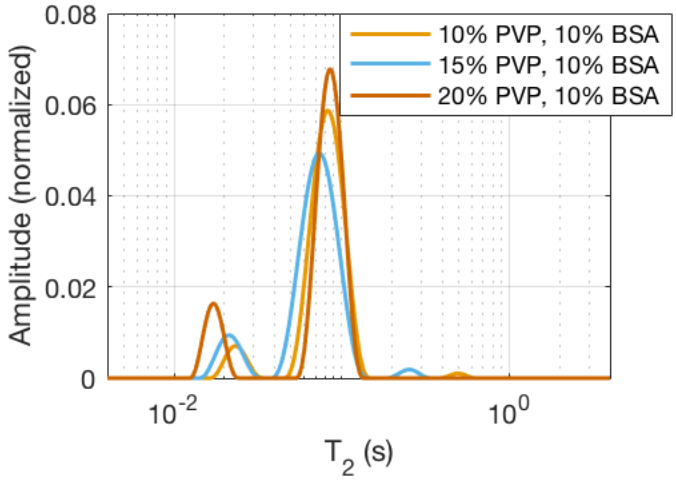

Figure 3.3: Representative T_2 spectra for cross-linked PVP:BSA phantoms at three PVP concentrations. Short-lived PVP proton signal accounts for 4.7 %, 9.0 % and 14.2 % of the total signal in 10 %, 15 % and 20 % PVP phantoms, respectively.

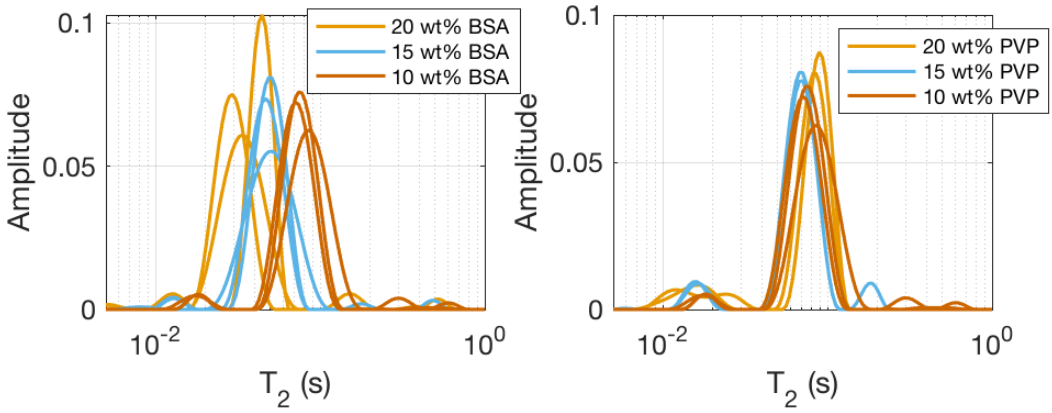

Figure 3.4: T_2 spectra comparison between (left) 10 wt% PVP phantoms of varying BSA composition and (right) 10 wt% BSA phantoms of varying PVP composition. Increasing BSA concentration shifts the largest signal component left, while increasing PVP concentration has little effect.

BSA cross-linking further reduces water diffusion in the phantoms compared to that of PVP alone in solution (Fig 3.7), but restrictions on PVP concentration result in a narrower range of apparent diffusion coefficients (minimum 1.0 μm^2/ms at 23 °C). There is a strong correlation between both

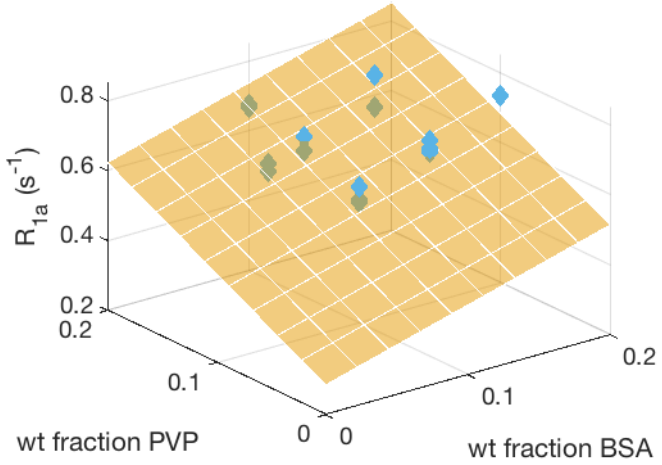

Figure 3.5: Plot of R_1 relaxation rate vs. PVP and BSA concentrations.

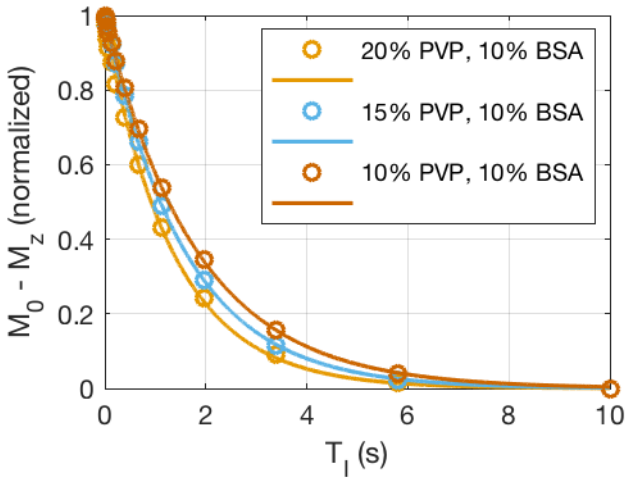

Figure 3.6: Plot of T_1 relaxation expressed as magnetization M_z subtracted from equilibrium vs. inversion time T_I. Solid lines represent best-fit mono-exponential decay curves.

chemical concentrations and measured apparent diffusion coefficient (ADC, adjusted $R^2 = 0.97$). As with the phantoms' relaxometry characteristics, the apparent diffusion of water in PVP:BSA is best represented by a two-compartment model in PVP:BSA. Across all concentrations studied, the two compartment model described by Eq. 2.1 was found to be a better fit when compared to a mono-exponential decay (all calculated F-statistics > 8, $p < 0.01$). The reasoning for fitting the data in this way and an explanation of potential bias in ADC measurements based on acquisition parameters and phantom composition are provided in the Discussion. While not in perfect agreement, parameters T_1 and T_2 obtained by fitting diffusion signal to Eq. 2.1 approximate the values obtained in relaxometry

analysis (Table 3.1). These differences are in part attributable to the differences in field strength and refocusing rate between the two measurements, which may affect the observed T_2 on their own.

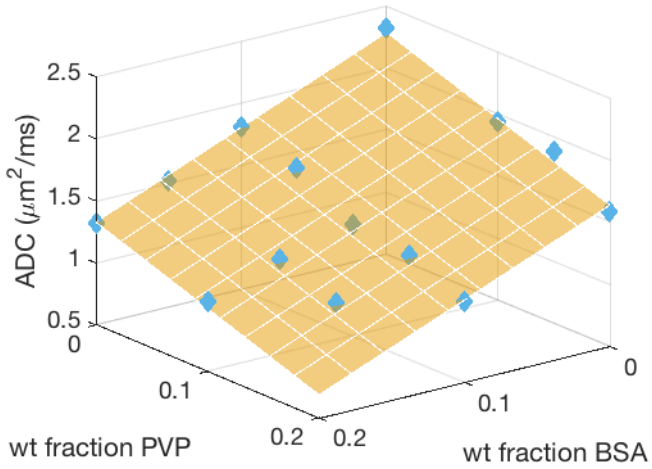

Figure 3.7: Plot of ADC vs. PVP and BSA concentration for cross-linked PVP:BSA phantoms. Data points represent mean ADC across three phantoms. Semi-transparent surface represents predicted ADC using the model described by Eq. 3.5

Table 3.1: Comparison of T_1 and T_2 parameters as fitted using Eq. 2.1 with relaxometry measurements at 23 °C and 7 T.

X_{PVP}	X_{BSA}	**Relaxometry** T_{2a} **(ms)**	**Diffusometry** T_{2a} **(ms)**	**Relax.** T_{2b} **(ms)**	**Diff.** T_{2b} **(ms)**
10	**10**	81.3	60.7	21.3	9.7
10	**15**	48.4	43.4	8.7	10.5
10	**20**	35.6	32.4	—†	11.5
15	**10**	70.9	73.4	20.5	9.9
15	**15**	46.2	40.3	—†	9.9
20	**10**	61.6	48.6	11.7	9.7

† Unable to distinguish two components by T_2 relaxometry

Finally, a tissue-relevant magnetization transfer effect is observed in the cross-linked phantoms, but not in phantoms which contain PVP alone (Fig. 3.8). Note the contrast between the bi-exponential PVP:BSA signal recovery curve and the mono-exponential aqueous PVP curve at 30 ms and below. From this, it can be inferred that the chemically shifted PVP proton signal is uninvolved in the exchange process with water. The observed bound pool fraction linearly correlates to BSA proportion (adjusted R^2 = 0.91), and is independent of PVP concentration for water content above 70% by mass. Within this restriction, it is possible to target a bound pool fraction of approximately 0.06 to 0.12 as described by Eq 3.6 (adjusted R^2 = 0.911). Off-resonance irradiation results indicate

that the MT effect observed in these phantoms is symmetric (Fig 3.9). One exception occurs in the frequency offset range 200 to 1000 Hz, where signal differs from 1 to 3 % between the two offset directions due to the presence of chemically shifted PVP proton signal. Furthermore, the water magnetization curves plotted as a function of frequency offset within these phantoms differs in shape from the sigmoidal curves produced by modeling a system with comparable relaxation rates and no magnetization exchange. These phantoms, then, should also produce an observable, tissue-relevant magnetization transfer effect when probed using off-resonance qMT sequences.

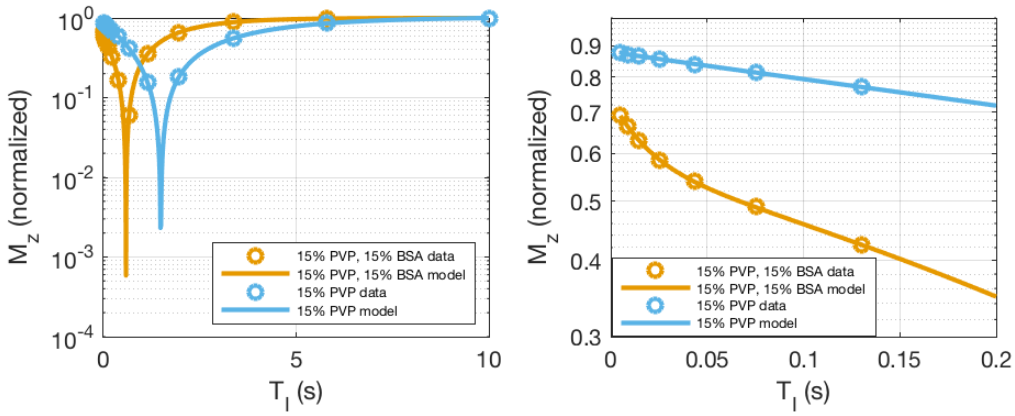

Figure 3.8: (Left) Plot of selective inversion recovery signal vs. inversion time for a cross-linked 15% PVP, 15% BSA phantom and an aqueous 15% PVP phantom. (Right) SIR signal recovery plot zoomed in to highlight bi-exponential recovery of the cross-linked phantom

3.2.2 Model and Equations

In totality, a model of this phantom is presented graphically in Fig 3.10, and equations relating each model parameter to concentrations of PVP and BSA as well as static magnetic field strength are provided in Eqs 3.1–3.6. No statistically significant ($p < 0.05$) interaction terms between independent variables were found for any of the relationships described. Within the range of compositions studied and at 23 °C, it is possible to simultaneously control 1) apparent diffusion coefficients from 1.0 - 1.8 μm^2/ms, 2) T_1 from 1.2 - 1.9 s at 9.4 T, 3) bound pool signal proportion from 6-12 %, 4) free water T_2 from 45 - 90 ms, and 5) short-lived T_2 from 8 - 25 ms.

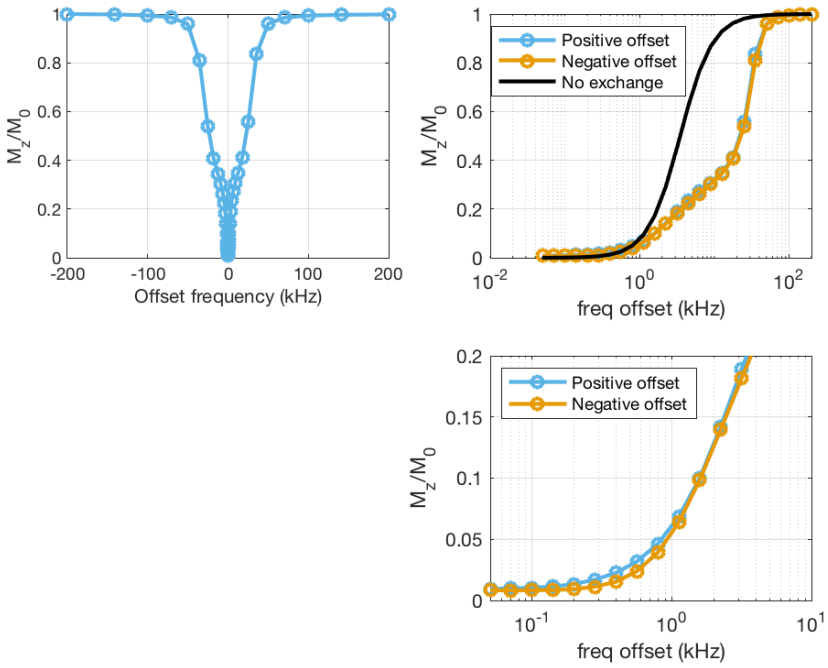

Figure 3.9: (Left) Plot of magnetization M_z vs. offset frequency for a cross-linked 15% PVP, 15% BSA phantom. (Top right) M_z vs. positive and negative offset frequency curves plotted together for direct comparison. The solid black curve represents the signal model for a system with $T_1 = (1.4\text{ s})$ and $T_2 = 40$ ms in the absence of magnetization exchange. (Bottom right) Magnetization vs. frequency offset curves zoomed in to highlight signal discrepancy at the frequency offset where PVP signal can be found.

$$R_{2a} = r_{2a,0} + r_{2a,B}X_{BSA} \tag{3.1}$$

$$R_{2b} = r_{2b,0} + r_{2b,H}X_{PVP} \tag{3.2}$$

$$f_b = f_{b,0} + f_{b,P}X_{PVP} \tag{3.3}$$

$$R_{1a} = r_{1,0} + r_{1,P}X_{PVP} + r_{1,B}X_{BSA} \tag{3.4}$$

$$D_a = d_0 + d_P X_{PVP} + d_B X_{BSA} \tag{3.5}$$

$$f_m = f_{m,0} + f_{m,B}X_{BSA} \tag{3.6}$$

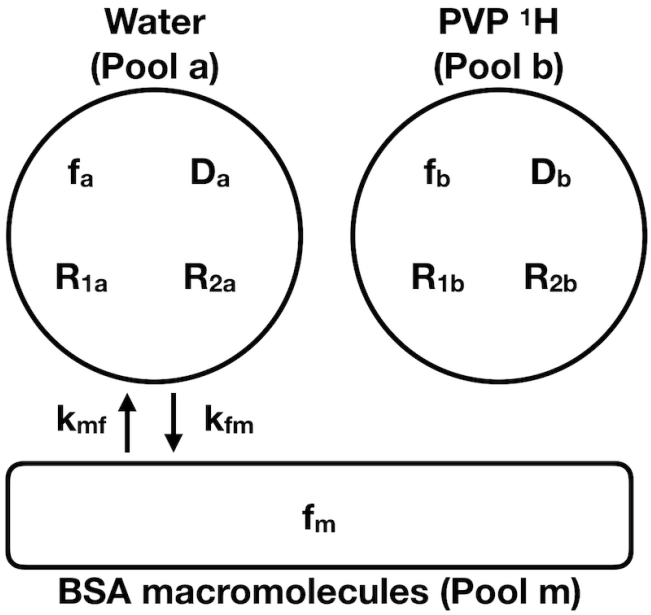

Figure 3.10: Model of the PVP:BSA phantom system. MR signal sources from three major pools: 1) water protons (denoted pool a), 2) protons on the PVP polymer chain (denoted pool b), and 3) macromolecular protons introduced by BSA (denoted pool m).

3.2.3 Reproducibility

Table 3.3 lists the mean and standard deviation of measured qMRI parameters across three phantoms. T_1, f_m, and ADC were consistent across phantoms, with standard deviations well under 5% of their mean values. T_{2a} and T_{2b} are equally consistent between phantoms when two components can be easily observed; in cases where differentiating between the pools is impossible, there is greater variation in T_2 measurement. A short-lived pool can be reliably reproduced with T_2 = 10 to 25 ms, and f_b is controllable to within approximately 1-2% of the total measured signal, provided the total water content is greater than 70 % by mass.

Table 3.2: Fitted constants for Equations 3.1–3.6. Values represent mean plus or minus standard error.

Parameter Name	**Value**	**Units**
$r_{2a,0}$	3.395 ± 1.333	s^{-1}
$r_{2a,B}$	95.009 ± 11.541	s^{-1}
$r_{2b,0}$	38.569 ± 3.086	s^{-1}
$r_{2b,P}$	85.011 ± 21.383	s^{-1}/T
$f_{b,0}$	-0.030 ± 0.014	—
$f_{b,P}$	0.897 ± 0.105	—
$r_{1,0}$	0.282 ± 0.035	s^{-1}
$r_{1,P}$	1.737 ± 0.150	s^{-1}
$r_{1,B}$	1.055 ± 0.188	s^{-1}
d_0	2.213 ± 0.057	$\mu m^2/ms$
d_P	-4.374 ± 0.356	$\mu m^2/ms$
d_B	-3.074 ± 0.207	$\mu m^2/ms$
$f_{m,0}$	0.0098 ± 0.0095	—
$f_{m,B}$	0.539 ± 0.068	—

Table 3.3: PVP:BSA phantom data at 23 °C. T_1 and T_2 were measured at 9.4 T.

Wt% PVP	**Wt% BSA**	**T_{1a} (ms)**	**T_{2a} (ms)**	**T_{2b} (ms)**	**f_b**	**f_m**	**ADC (μm^2/ms)**
10	**10**	1783 ± 72	81.3 ± 3.6	21.3 ± 0.5	.060 ± .018	0.062 ± 0.003	1.393 ± 0.071
15	**10**	1548 ± 40	70.9 ± 2.3	20.5 ± 0.4	0.105 ± 0.009	0.062 ± 0.001	1.264 ± 0.065
10	**20**	1357 ± 20	35.6 ± 5.1	—	—	0.115 ± 0.014	1.147 ± 0.017

Chapter 4. Discussion

Here we have interrogated the PVP:BSA system as a multi-modal qMRI phantom and reported tissue-relevant characteristics for T_1, multi-exponential T_2, magnetization transfer, and diffusion of water. The following sections first discuss limitations in phantom synthesis, then further explore the qMRI parameter trends and model equations outlined in the Results.

4.1 Phantom Production Limitations

The range of PVP and BSA compositions studied were chosen after encountering specific issues at each border. Below the studied range of PVP and BSA composition, cross-linking is not observed, and the solution remains in a liquid state. It is recommended to use at least 10% BSA by mass to ensure that cross-linking is successful and a homogeneous structure forms. On the other end, reducing the water content below 70% by mass has two negative effects which impede phantom preparation. First, BSA becomes more difficult to dissolve, and will form a precipitate in solution. Increasing the solution's temperature during mixing and carefully dissolving BSA slowly over time can help alleviate this near the proposed limit, but the phantoms have one more noteworthy limitation at low water content. The microwave cross-linking procedure produces air bubbles in the phantoms which must escape before the structure sets. As the water content drops to 70% by mass and below, the solution becomes too viscous for air bubbles to escape before cross-linking finishes. Using three short doses of microwave irradiation rather than one long one alleviates this issue when the water content is high enough, but air bubbles should be expected if PVP and BSA concentration rise enough.

Two other simple cross-linking procedures were entertained, but both have their own issues. Cross-linking via heat over the course of 10 to 20 minutes is possible, but this has only been shown to work for BSA; during this time the BSA cross-links with itself and forms a phase apart from PVP, resulting in an inhomogeneous, undesirable solution. Glutaraldehyde and similar chemical cross-linking agents work primarily on BSA, causing it to cross-link with itself apart from PVP. Vortexing the solution while it cross-links homogenizes it, but at high PVP concentrations this also forms

trapped air bubbles. Perhaps a more complex cross-linking procedure could work around these obstacles, but as our purpose was to develop an inexpensive, simple-to-make set of phantoms, attempts to further refine the cross-linking procedure are outside the scope of this paper and should be the focus of future studies.

If more restricted diffusion is desired, ADC can be further reduced by scanning phantoms at a lower temperature, or by substituting greater concentrations of aqueous PVP (i.e. without BSA). Note that using aqueous PVP will remove the magnetization transfer effect.

4.2 ^{1}H NMR and Signal Characterization

The number and location of chemically shifted peaks observed in Figure 3.1 are comparable to higher-resolution data acquired by Loría-Bastarrachea et al. in 2011 [19]. To our knowledge, there are no publications to date that have separated aqueous PVP into components based on T_1 and T_2 relaxometry. In part, this is due to the general focus on PVP as a diffusion phantom, and less commonly as a T_1 phantom [20]. Additionally, the short T_2 relaxation times of PVP protons make them difficult to identify without protocols involving short echo time acquisition, particularly for the high PVP concentrations most relevant to restricted diffusion studies.

4.3 Relaxation

The separate roles PVP and BSA play in determining multi-exponential T_2 can be explained by investigating the cross-linking procedure and identifying the separate sources of observed signal. First, it must be noted that the microwave cross-linking procedure cannot be accomplished in the absence of BSA. It is essentially a rapid version of another well-documented BSA cross-linking procedure in which aqueous BSA is heated at approximately 80 °C for 10 to 15 minutes [21]. The phantoms' structural change drastically reduces water mobility and T_2 of the observed signal. Figure 4.1 displays R_2 as a function of PVP composition in aqueous phantoms without any added BSA. In these phantoms, no cross-linking can occur, and T_{2a} is longer than 1 second for 10 wt% PVP at 9.4 T. Compared to the drastic T_2 change involved in cross-linking PVP:BSA phantoms, PVP's effect

on observed T_{2a} is negligible, especially in the 10-20 wt% PVP range. However, since PVP protons are the source of the short-lived MR signal, PVP concentration is solely responsible for the size of the short-lived signal pool. Furthermore, the mobility of protons on the PVP chain is already restricted, so the cross-linking procedure has little effect on T_{2b}. Reported measurements of T_2 relaxation time are generally a single value close to what is reported here for pool a [4].

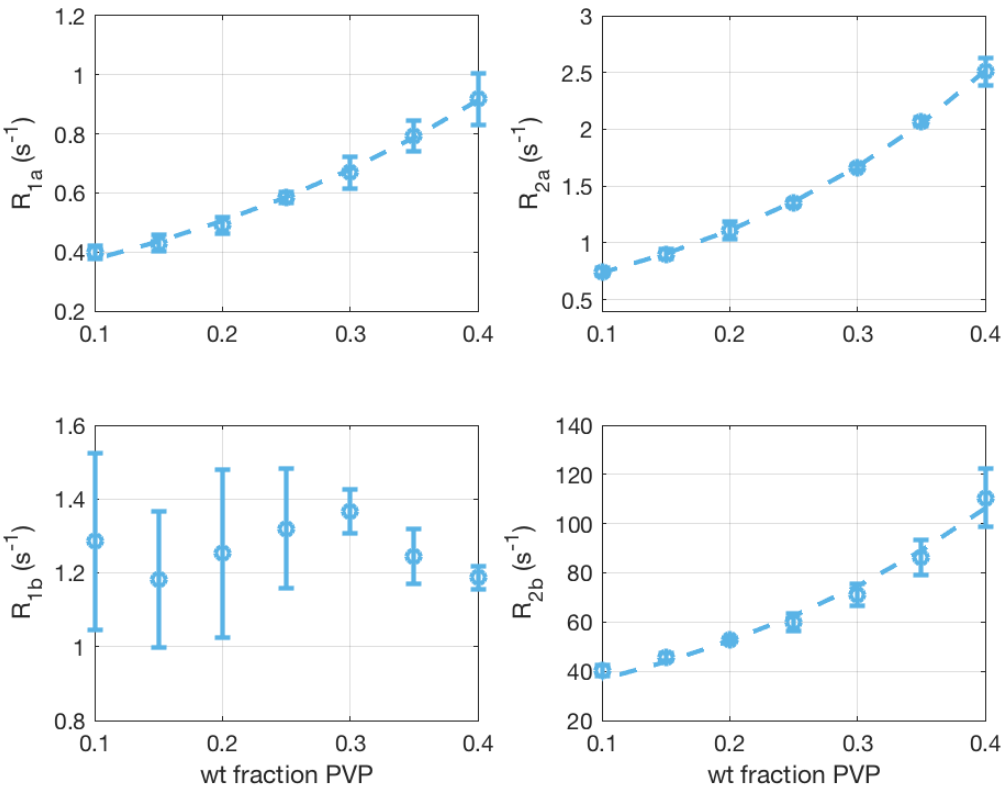

Figure 4.1: R_1 (left) and R_2 (right) relaxation rates of the two major signal components (pool a, top; pool b, bottom) plotted against PVP weight fraction. Data points represent mean ± standard deviation across three phantoms. Dashed lines represent best-fit exponential models.

4.4 Magnetization Transfer

Reported bound pool fraction values are similar to literature data from aqueous BSA phantoms with the same BSA mass fractions; further, the linear relationship between BSA content and bound pool fraction has been previously recorded in other cross-linked BSA phantoms [22]. Slight differences in BPF are expected, since the cross-linking procedure used in this study differs from the

slow-heating and chemical cross-linking methods used in most prior MT characterizations of aqueous BSA. The trend of observed magnetization M_z as a function of frequency offset reported in figure 3.9 differs from the sigmoidal curve expected in the absence of magnetization exchange [15], supporting the nonzero MT effect fitted in PVP:BSA using SIR data. If PVP protons were contributing to this exchange, one would expect to see bi-exponential recovery in the aqueous PVP phantom (Fig 3.8).

The insignificant effect of PVP concentration on bound pool fraction reported here may be explained by further exploring the chemical system. SIR sequences typically fit signal to a bi-exponential model like the following:

$$M_f(t)/M_{f\infty} = b_f^+ e^{-R_1^+ t} + b_f^- e^{-R_1^- t} + 1. \tag{4.1}$$

Here, signal recovery is separated into contributions from a long-lived water signal component (−) and a short-lived macromolecular component (+). In the case of PVP:BSA, protons source from three pools: water, BSA macromolecules, and PVP protons. A more accurate representation of this system would be

$$M_f(t)/M_{f\infty} = b_f^+ e^{-R_1^+ t} + b_f^- e^{-R_1^- t} + b_f^{\mathrm{P}} e^{-R_1^{\mathrm{P}} t} + 1. \tag{4.2}$$

The PVP protons decay with $R_1 \approx 1.5\,\mathrm{s}^{-1}$, a rate much closer to R_1^- than to R_1^+. As a result, PVP magnetization is lumped in with water magnetization when fitting to a bi-exponential, and the fraction of signal belonging to BSA only changes with BSA concentration.

The signal discrepancy between frequency offset directions around 200 to 1000 Hz shows that PVP protons can be responsible for slight signal fluctuations in qMT signal. However, this difference is small ($< 5\,\%$ of observed signal) and most of the differences in the M_z vs frequency offset curves due to magnetization transfer are observed at greater frequency offsets (Fig 3.9). The symmetry observed beyond 1000 Hz when changing the frequency offset direction indicates that the phantoms exhibit a homogeneous magnetization transfer effect resulting from interactions between water and BSA macromolecular protons.

4.5 Diffusion

Prior publications have reported mono-exponential behavior of diffusion-weighted signal in PVP phantoms independent of diffusion time [10, 14, 23]. These reports and the trends identified here can be compatible if we consider the sources of MR contrast in PVP. Most diffusion-weighted imaging analyses in tissue will fit signal to an exponential decay function to fit one ADC value. The PVP phantom signal, however, includes contributions from longer-lived water signal and shorter-lived signal from protons on the PVP chain (discussed in the Relaxation subsection). Since the effectively immobile PVP proton signal does not decay as b-value increases, a constant term would be added to the signal model. Figure 4.2 illustrates this concept; at longer echo times and greater PVP concentrations, the signal decay curve tends toward mono-exponential behavior. However, if enough PVP proton signal remains during acquisition, the signal decay curve approaches a non-zero constant as b-value increases. As long as the b-value used in fitting remains low enough, the constant term is small relative to the total recorded signal, so fitted ADC values are not significantly affected. Future diffusion studies which use PVP should be aware of this immobile signal, with the following practical implications. First, if the PVP concentration is high, the T_2 of the immobile signal is short enough that it becomes irrelevant, even for studies on animal systems with relatively short T_E. Otherwise, if the b-values used in data fitting are small ($\leq$ 1500 s/mm^2), the immobile signal effect is also negligible. If high b-values are used, and if PVP proton signal survives to acquisition, the fitted ADC will be skewed downward.

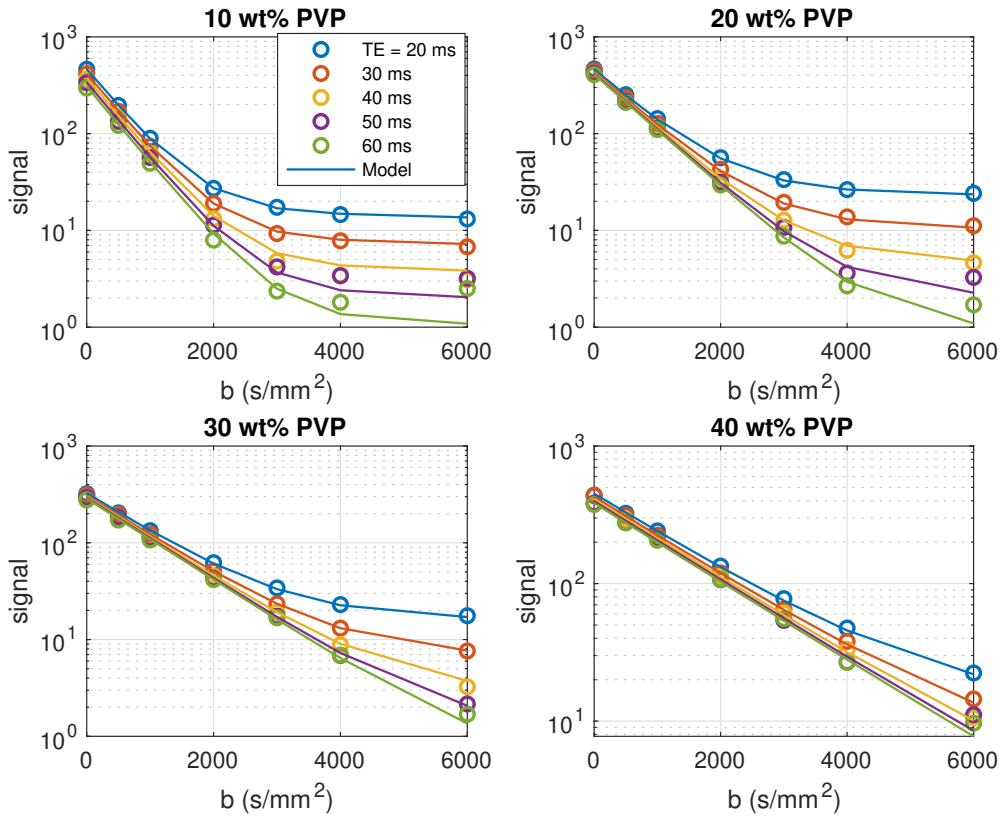

Figure 4.2: Mean signal vs. b-value plots of 10-40 wt% PVP phantoms from diffusion-weighted images acquired at multiple time points after excitation. Mono-exponential signal decay is observable at large PVP concentrations and long echo times, but cannot fully describe signal recorded from lower PVP concentrations and shorter echo times.

Chapter 5. CONCLUSIONS AND FUTURE WORK

5.1 Conclusions

In the preceding chapters we have characterized cross-linked PVP:BSA systems with respect to their T_1 and T_2 relaxation, magnetization transfer, and apparent water diffusion characteristics using non-localized ^{1}H NMR and imaging experiments. We have identified an observable short T_2 signal pool in PVP which decays at a similar rate to the trapped water component found in myelinated tissue, establishing aqueous PVP as an inexpensive and easily-prepared solution for multi-exponential T_2 qMRI studies. Furthermore, we have demonstrated that cross-linked polyvinylpyrrolidone:bovine serum albumin phantoms are capable of simultaneously producing 1) a controllable range of tissue-relevant diffusion coefficients, 2) relevant multi-exponential T_2 and T_1 behavior, and 3) an MT effect comparable to the gray and white matter tissue range. Phenomenological models for qMRI parameters as they relate to phantom composition have been provided where applicable.

5.2 Future Work

The chemical systems characterized in this work have great potential as multi-parametric qMRI phantoms, but a few further steps should be taken to increase the phantoms' applicability and improve standardization across sites. With respect to applicability, the clear next step is to extend this characterization to lower field strengths, particularly to better describe relaxation rates. Additionally, some changes in phantom preparation—particularly in the imaging container used when cross-linking samples—may be implemented when using these phantoms on larger-bore human systems. While such alterations to the preparation scheme should not be expected to change any characteristics of the sample, it remains to be seen how well the microwave cross-linking procedure works on solutions in differently-shaped containers, particularly with respect to homogeneity in the end product. The cross-linking procedure itself will require more thorough analysis to improve phantom standardization between sites. Microwave cross-linking was chosen primarily because it takes place

on a much smaller time scale than heating in a bath (preventing the separation of liquid PVP from cross-linked BSA), requires no chemical additives, does not necessitate rapid stirring to cross-link an entire sample, and only involves equipment which is readily available at most research institutions. However, it is currently unclear what changes to the microwave's power or irradiation time may have on the phase behavior and qMRI properties of the phantom system. The power used in this work is attainable by most conventional microwaves, but for standardization between sites to be assured, further experiments should be conducted at different power settings. The best outcome of such experiments would be an equation relating power to irradiation time needed to produce the same phantom structure, or else a more detailed list of properties as a function of irradiation power.

Chapter 6. Bibliography

[1] J. C. Blechinger, E. L. Madsen, and G. R. Frank. Tissue-mimicking gelatin–agar gels for use in magnetic resonance imaging phantoms. *Medical Physics*, 15(4):629–636, 1988.

[2] J. O. Christoffersson, L. E. Olsson, and S. Sjöberg. Nickel-doped agarose gel phantoms in mr imaging. *Acta Radiologica*, 32(5):426–431, 1991. PMID: 1911001.

[3] Hirokazu Kato, Masahiro Kuroda, Koichi Yoshimura, Atsushi Yoshida, Katsumi Hanamoto, Shoji Kawasaki, Koichi Shibuya, and Susumu Kanazawa. Composition of mri phantom equivalent to human tissues. *Medical Physics*, 32(10):3199—3208, October 2005.

[4] Kathryn E. Keenan, Lisa J. Wilmes, Sheye O. Aliu, David C. Newitt, Ella F. Jones, Michael A. Boss, Karl F. Stupic, Stephen E. Russek, and Nola M. Hylton. Design of a breast phantom for quantitative mri. *Journal of Magnetic Resonance Imaging*, 44(3):610–619, 2016.

[5] Hans. J Laubach, Peter M Jakob, Karl O Loevblad, Alison E Baird, Maria Picone Bovo, Robert R Edelman, and Steven Warach. A phantom for diffusion-weighted imaging of acute stroke. *Journal of Magnetic Resonance Imaging*, 8(6):1349–1354, 1998.

[6] Seymour H. Koenig, Rodney D. Brown III, and Raphael Ugolini. Magnetization transfer in cross-linked bovine serum albumin solutions at 200 mhz: A model for tissue. *Magnetic Resonance in Medicine*, 29(3):311–316, 1993.

[7] Craig Jones, Alex MacKay, and Brian Rutt. Bi-exponential t2 decay in dairy cream phantoms. *Magnetic Resonance Imaging*, 16(1):83–85, 1998.

[8] R. Adam Horch and Mark D. Does. Aqueous urea as a model system for bi-exponential relaxation. *Magnetic Resonance Materials in Physics, Biology and Medicine*, 20(1):51, 2007.

[9] Robert L. Vold, E. S. Daniel, and S. O. Chan. Magnetic resonance measurements of proton exchange in aqueous urea. *Journal of the American Chemical Society*, 92(23):6771–6776, 1970.

[10] Kathryn E. Keenan, Maureen Ainslie, Alex J. Barker, Michael A. Boss, Kim M. Cecil, Cecil Charles, Thomas L. Chenevert, Larry Clarke, Jeffrey L. Evelhoch, Paul Finn, Daniel Gembris, Jeffrey L. Gunter, Derek L.G. Hill, Clifford R. Jack Jr., Edward F. Jackson, Guoying Liu, Stephen E. Russek, Samir D. Sharma, Michael Steckner, Karl F. Stupic, Joshua D. Trzasko, Chun Yuan, and Jie Zheng. Quantitative magnetic resonance imaging phantoms: A review and the need for a system phantom. *Magnetic Resonance in Medicine*, 79(1):48–61, 2018.

[11] Akifumi Hagiwara, Masaaki Hori, Julien Cohen-Adad, Misaki Nakazawa, Yuichi Suzuki, Akihiro Kasahara, Moeko Horita, Takuya Haruyama, Christina Andica, Tomoko Maekawa, et al. Linearity, bias, intrascanner repeatability, and interscanner reproducibility of quantitative multidynamic multiecho sequence for rapid simultaneous relaxometry at 3 t: a validation study with a standardized phantom and healthy controls. *Investigative Radiology*, 54(1):39–47, 2019.

[12] Gregory Lemberskiy, Els Fieremans, Dmitry S Novikov, and Martijn Cloos. Quantitative validation of spin echo and magnetic resonance fingerprinting derived proton density using the qmri phantom. Proceedings of the International Society for Magnetic Resonance in Medicine, 2017.

[13] E M Palacios, A J Martin, M A Boss, F Ezekiel, Y S Chang, E L Yuh, M J Vassar, D M Schnyer, C L MacDonald, K L Crawford, A Irimia, A W Toga, and P Mukherjee. Toward precision and reproducibility of diffusion tensor imaging: A multicenter diffusion phantom and traveling volunteer study. *AJNR Am J Neuroradiol*, 38(3):537–545, Mar 2017.

[14] Carlo Pierpaoli, Joelle Sarlls, Uri Nevo, Peter Basser, and Ferenc Horkay. Polyvinylpyrrolidone (pvp) water solutions as isotropic phantoms for diffusion mri studies. *Proceedings of the International Society for Magnetic Resonance in Medicine*, 17, 01 2009.

[15] R. Mark Henkelman, Xuemei Huang, Qing-San Xiang, G. J. Stanisz, Scott D. Swanson, and Michael J. Bronskill. Quantitative interpretation of magnetization transfer. *Magnetic Resonance in Medicine*, 29(6):759–766, 1993.

[16] K Whittall and A MacKay. Quantitative interpretation of NMR relaxation data. *Journal of Magnetic Resonance (1969)*, 84(1):134 152, 1989.

[17] Daniel F. Gochberg and John C. Gore. Quantitative magnetization transfer imaging via selective

inversion recovery with short repetition times. *Magnetic Resonance in Medicine*, 57(2):437–441, 2007.

[18] Ke Li, Zhongliang Zu, Junzhong Xu, Vaibhav A. Janve, John C. Gore, Mark D. Does, and Daniel F. Gochberg. Optimized inversion recovery sequences for quantitative t1 and magnetization transfer imaging. *Magnetic Resonance in Medicine*, 64(2):491–500, 2010.

[19] M. Loría-Bastarrachea, Wilberth Herrera, Juan Cauich, Humberto Vázquez, Alejandro Avila-Ortega, and Manuel Cervantes. A tg/ftir study on the thermal degradation of poly(vinyl pyrrolidone). *Journal of Thermal Analysis and Calorimetry*, 104:737–742, 05 2011.

[20] Dan Benjamini and Peter J. Basser. Use of marginal distributions constrained optimization (madco) for accelerated 2d mri relaxometry and diffusometry. *Journal of Magnetic Resonance*, 271:40 – 45, 2016.

[21] Daniel F. Gochberg, Richard P. Kennan, Matthew D. Robson, and John C. Gore. Quantitative imaging of magnetization transfer using multiple selective pulses. *Magnetic Resonance in Medicine*, 41(5):1065–1072, 1999.

[22] Daniel F. Gochberg and John C. Gore. Quantitative imaging of magnetization transfer using an inversion recovery sequence. *Magnetic Resonance in Medicine*, 49(3):501–505, 2003.

[23] Friedrich Wagner, Frederik B. Laun, Tristan A. Kuder, Anna Mlynarska, Florian Maier, Jonas Faust, Kerstin Demberg, Linus Lindemann, Boris Rivkin, Armin M. Nagel, Mark E. Ladd, Klaus Maier-Hein, Sebastian Bickelhaupt, and Michael Bach. Temperature and concentration calibration of aqueous polyvinylpyrrolidone (pvp) solutions for isotropic diffusion mri phantoms. *PLoS One*, 12(6):1–13, 06 2017.

[24] Young S. Kang, John C. Gore, and Ian M. Armitage. Studies of factors affecting the design of NMR contrast agents: manganese in blood as a model system. *Magnetic Resonance in Medicine*, 1(3):396–409, sep 1984.

[25] Rustem R. Amirov, Evgenia A. Burilova, Zuleykha T. McMillan, Lyaysan R. Amirova, Anna B. Ziyatdinova, Julia R. Shayimova, Mikhail S. Bukharov, Airat M. Dimiev, and Alexei V. Zakharov. An nmr relaxivity and esr study of the interaction of the paramagnetic manganese(ii)

and gadolinium(iii) ions with anionic, cationic and neutral water-soluble polymers and their mixtures. *Journal of Molecular Liquids*, 238:184 – 192, 2017.

[26] Kalaivani Thangavel and Emine Saritas. Aqueous paramagnetic solutions for mri phantoms at 3 t:a detailed study on relaxivities. *Turkish Journal of Electrical Engineering & Computer Sciences*, 25:2108–2121, 01 2017.

Appendices

Appendix A. Characterization of Aqueous PVP

Although aqueous PVP lacks a tissue-relevant magnetization transfer effect, it has (to the best of our knowledge) heretofore undocumented potential as a multi-exponential T_2 phantom, and is capable of producing relevant qMRI parameters in every other characteristic explored in this work. As such, a characterization of aqueous PVP phantoms including multi-exponential T_2, T_1, and water diffusion is provided here.

A.1 Characterization

A.1.1 Relaxation

Figure 4.1, presented in this work's main body, plots the relaxation rates R_1 and R_2 against PVP composition by mass. When changing the PVP concentration, the relaxation rates R_{1a}, R_{2a}, and R_{2b} increase exponentially with increasing PVP weight fraction (Fig. 4.1). This relationship is modeled according to the equation

$$R = C_1 e^{C_2 \cdot X_{\mathrm{PVP}}}. \tag{A.1}$$

Here R represents the relaxation rate measured in s^{-1} and X_{PVP} is the weight fraction of PVP. Table A.1 lists the coefficients in each exponential fit equation. R_{1b} exhibits the greatest variance between phantoms and does not change significantly with PVP concentration.

Table A.1: Fitted parameters describing the relationship between relaxation rates and concentration of PVP at 9.4T (equation A.1). 95% confidence intervals are in parentheses.

	C_1 (s-1)	C_2
R1a (s-1)	0.2794 (0.2495, 0.3092)	2.962 (2.626, 3.297)
R2a (s-1)	0.490 (0.460, 0.520)	4.09 (3.905, 4.275)
R2b (s-1)	25.79 (22.11, 29.46)	3.54 (3.103, 3.977)

If PVP is to be used as a multi-parametric tissue-relevant qMRI phantom, manganese chloride should be added to bring both relaxation times into a tissue-relevant range. Lower PVP compositions allow manganese chloride to reduce T_2 to a relevant time without sacrificing tissue relevance in T_1; 10 wt% PVP phantoms are recommended for simultaneous T_1 and multi-exponential T_2 behavior in an aqueous PVP phantom. Figure A.1 plots the relaxation rates R_1 and R_2 against manganese concentration in 10 wt% PVP phantoms. Table A.2 lists the relaxivity coefficients r_1 and r_2, calculated as the slope of the best fit lines in Fig. A.1 recorded at 7.0 T and 9.4 T.

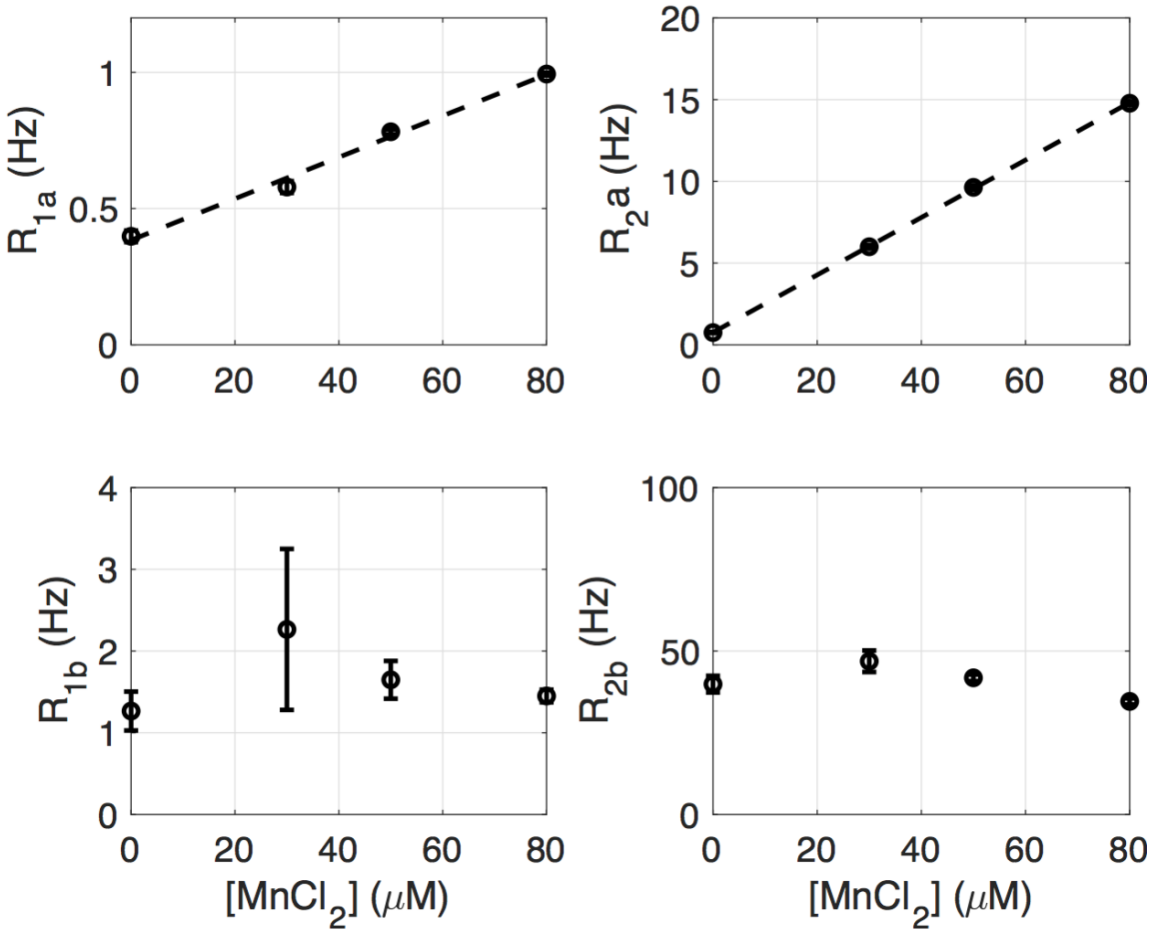

Figure A.1: R1 (left) and R2 (right) relaxation rates of the two major signal components (pool A, top; pool B, bottom) plotted against manganese(II) chloride concentration. Data points represent mean ± standard deviation across three phantoms. Dashed lines represent lines of best fit.

Table A.2: Relaxivities r_1 and r_2 of manganese chloride in 10 wt% PVP phantoms. Values in parentheses mark 95% confidence interval.

Field Strength (T)	$\mathbf{r_1}$ **(mM^{-1}s^{-1})**	$\mathbf{r_2}$ **(mM^{-1}s^{-1})**
7.0 T	6.064 (5.725, 6.403)	161.7 (148.5, 174.9)
9.4 T	7.603 (7.024, 8.183)	175.8 (173.3, 178.2)

A.1.2 Diffusion

Aqueous PVP phantoms are capable of producing lower apparent diffusion coefficients than what is allowed in the PVP:BSA formulation characterized in the main body. The fitted ADC values (D_a from Equation 2.1) are plotted against PVP concentration in Figure A.2. The relationship remains approximately linear from 20% to 40% PVP by mass. Within this regime, the diffusion coefficient can be related to the weight fraction of PVP by Equation A.2.

$$D_{app} = C_1 X_{PVP} + C_2. \tag{A.2}$$

Here, D_{app} is the ADC of water measured in $\mu m^2/ms$ and X_{PVP} is the weight fraction of PVP. At 23 °C, 95% confidence intervals set C_1 = -3.445 ± 0.210 μm^2/ms and C_2 = 1.993 ± 0.064 μm^2/ms.

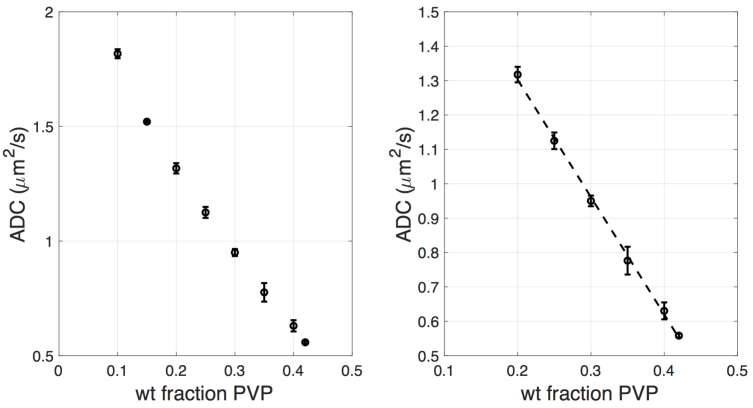

Figure A.2: Left: plot of apparent diffusion coefficient vs. PVP concentration across entire studied range. Right: subset of PVP concentrations which exhibit a linear relationship with measured ADC. Data points represent mean ± standard deviation. Dashed line represents line of best fit (R^2 = .990).

A.1.3 Other Field Strengths

Figure A.3 includes relaxation measurements for aqueous PVP phantoms acquired at 4.7 T, 7 T, and 9.4 T. The line relating R_1 to manganese concentration does not significantly change in slope between the three field strengths, but the y-intercept is affected. Equation A.3 below describes R_1 as a function of field strength and manganese chloride concentration:

$$R_1 = C_1[Mn] + C_2 B_0 \tag{A.3}$$

Fitting the data from all three field strengths to the above equation results in the following parameters with 95% confidence intervals: $C_1 = 8.086 \pm 0.863 mM^{-1}s^{-1}$ and $C_2 = 0.039 \pm 0.005 s^{-1}$. The effect of field strength on R_1 is small compared to the effect of manganese chloride concentration.

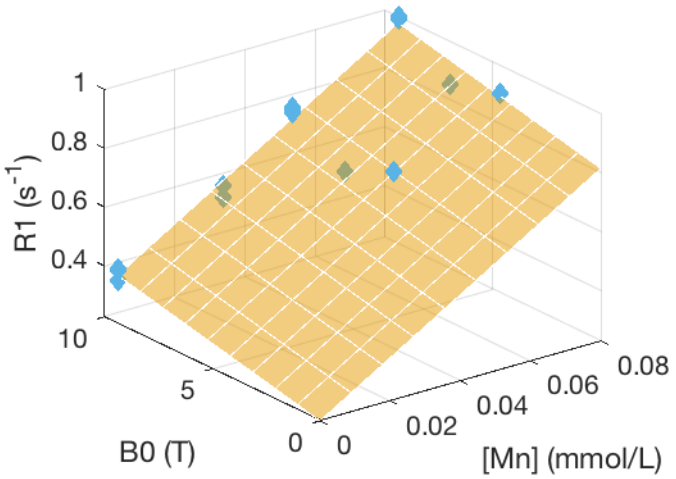

Figure A.3: Effect of field strength and manganese concentration on R1 of aqueous PVP phantoms.

With respect to R_2, PVP phantoms exhibit a linear relationship between the r_2 relaxivity (slope) and field strength. In the absence of manganese chloride, the change in R_2 with field strength is negligible. The following phenomenological equation describes R_2 as a function of field strength and manganese chloride concentration:

$$R_2 = B_0 C_1[Mn] + C_2 \tag{A.4}$$

The fitted parameters in equation A.4 with 95% confidence intervals are as follows: $C_1 = 18.36 \pm 1.15 mM^{-1}s^{-1}T^{-1}$ and $C_2 = 0.7613 \pm 0.5154 s^{-1}$.

A.2 Discussion

The exponential relationship between relaxation rates and PVP weight fraction in the aqueous PVP phantoms can be explained if we consider a "bound" pool of water protons closely interacting with PVP protons. Let M_p represent the mass of PVP and M_w represent the mass of water in a given phantom. The number of free water protons (n_a) is proportional to the water content, while the number of bound water protons (n_b) is proportional to the PVP content, as described in Equations A.5 and A.6 below.

$$n_a = \phi_a M_w \tag{A.5}$$

$$n_b = \phi_b M_p \tag{A.6}$$

Here, ϕ_a and ϕ_b are proportionality constants relating the number of protons in the free and bound water pools to the mass of water and PVP, respectively. If we assume that exchange is occurring between the two water pools is fast compared to the phantom's relaxation rate, we can express the R_2 relaxation rate of water as follows:

$$R_{2\mathrm{a}} = f_a R_{2\mathrm{a}} + f_b R_{2\mathrm{b}} = \frac{\phi_a M_w}{\phi_a M_w + \phi b M_p} R_{2\mathrm{a}} + \frac{\phi_b M_p}{\phi_a M_w + \phi b M_p} R_{2\mathrm{b}} \tag{A.7}$$

Figure A.4 illustrates how well the data are explained by the fast exchange model with and without the dilute assumption, that is, that bound water pool is insignificant in size compared to the free water pool. The exponential trends observed for R_1 and R_2 are well-described by the exchange model, particularly when no dilute assumption is made. The fitted data includes a bound water component with T_2 approximately equal to 90 μs.

Relaxometry studies involving manganese (II) chloride utilized 10 wt% PVP for two main reasons: 1) these phantoms have the longest measured T_1, allowing greater $MnCl_2$ concentrations to be added before relevance to tissue is lost, and 2) the relaxivity ratio r_2/r_1 of manganese in phantoms with PVP

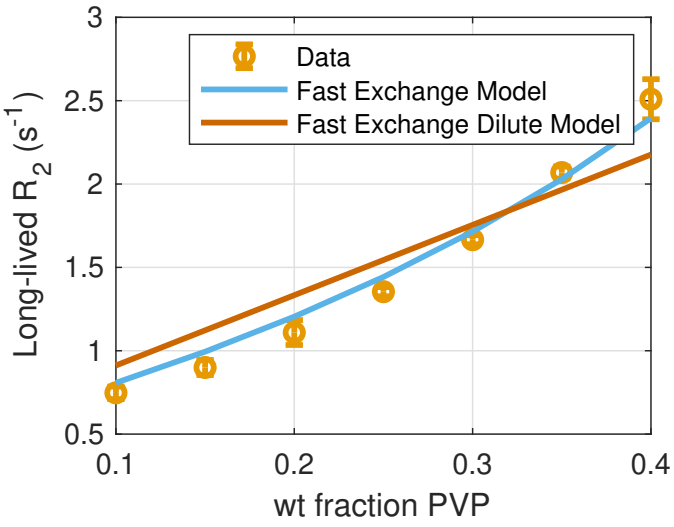

Figure A.4: R_2 relaxation rate of water signal in aqueous PVP phantoms. Solid lines represent two models based on fast exchange between bound and free water.

concentration above 25% is significantly lower than literature data from aqueous $MnCl_2$ phantoms. This difference is attributable to the binding of Mn^{2+} ions to sites on the PVP polymer; similar results have been observed for $MnCl_2$ interactions with proteins [24] and with longer PVP chains [25]. Phantoms at 20 wt% PVP and below exhibit similar r_2/r_1 behavior to reported data in aqueous $MnCl_2$ [26].

The diffusive behavior of aqueous PVP phantoms has been well-documented, including model equations as a function of PVP concentration and temperature. Pierpaoli et al. reported a similar linear relationship between ADC and PVP concentration between 15 and 50% PVP (in w/v) at 22 °C [14]. Wagner et al. reported an exponential relationship between temperature and apparent diffusion coefficient for aqueous PVP phantoms within the regime (15 °C ≤ T ≤ 25 °C) [23] Interpolating these results to 23 °C reveals good agreement with the ADC values reported here (maximum percent difference < 5%).

Appendix B. Aqueous PVP Parameter Tables

Table B.1: Aqueous PVP relaxometry and diffusometry data. Relaxometry measurements performed at 9.4 T. Diffusion measurements performed at 23 °C

Wt% PVP	$\mathbf{f_b}$	T_{1a} **(ms)**	T_{1b} **(ms)**	T_{2a} **(ms)**	T_{2b} **(ms)**	**ADC** (μ**m**^{2}**/ms)**
10	0.0645 ± 0.013	2515 ± 138	795 ± 135	1340 ± 66.0	24.9 ± 1.4	1.521 ± .004
15	0.104 ± 0.001	2330 ± 156	861 ± 138	1114 ± 56.7	21.9 ± 0.7	1.317 ± .022
20	0.140 ± 0.001	2040 ± 117	815 ± 141	904.2 ± 62.2	18.9 ± 0.4	1.126 ± .023
25	0.178 ± 0.004	1712 ± 57	766 ±100	738.7 ± 15.0	16.8 ± 1.0	0.950 ± .016
30	0.215 ± 0.002	1500 ±123	732 ± 31	600.4 ± 9.8	14.1 ± 0.9	0.777 ± .040
35	0.251 ± 0.001	1266 ± 85	805 ±48	483.5 ± 8.3	11.6 ± 1.0	0.631 ± .023
40	0.297 ± 0.009	1095 ± 99	843 ± 22	399.2 ± 0.97	9.1 ± 1.0	0.558 ± .004

Table B.2: Relaxometry measurements for 10 wt% PVP phantoms with added $MnCl_2$. Values represent mean ± standard deviation across three phantoms.

[Mn] (μ**M**)	T_{1a}	T_{1b}	T_{2a}	T_{2b}
0	2516 ± 138	807.3 ± 139.4	1341 ± 66	25.1 ± 1.6
30	1729 ± 66	530.9 ± 308.3	166.8 ± 3.2	21.4 ± 1.6
50	1279 ± 15	615.5 ± 93.8	103.8 ± 1.5	23.9 ± 1.6
80	1006 ± 5	690.8 ± 37.9	67.7 ± 0.6	28.9 ± 0.8